Equatorial ionospheric bubble precursor

M.J. Keskinen

Plasma Physics Division

Naval Research Laboratory

Washington, DC 20375

A time-dependent nonlinear three-dimensional model for the evolution of the equatorial bottomside lower ionosphere in the presence of dissipating gravity waves has been developed. From the numerical solution of the model, it is found that large bottomtype F-region ionospheric density perturbations and electric fields can be driven by dissipating gravity waves from tropospheric sources. The spatial distribution of the ionospheric F-region density perturbations can be characterized as a patchy, layer-like structure and may be responsible, in part, for observed large scale wavelike structures in the equatorial bottomside F-region which are a precursor to fully developed equatorial ionospheric bubbles. Favorable comparison of the model with observations is made.

1. Introduction

Spread-F bubbles frequently occur in the terrestrial ionosphere and are a major problem in ionosphere-thermosphere coupling and space weather forecasting. Spread-F bubbles refer to large holes in the ionospheric F-region plasma density. Recently, several studies both experimental [*Fritts et al.*, 2008; *Rodrigues et al.*, 2008; *Tsunoda*, 2006; *Hysell et al.*, 2005; *Kil et al.*, 2004; *Straus et al.*, 2003; *Abdu et al.*, **2009**; *Hocke and Tsuda*, 2001] and theoretical [*Huba et al.*, 2008; *Keskinen and Vadas*, 2009; *Hysell and Kudeki*, 2004; *Tsunoda*, 2006; *Bhattacharayya*, 2004; *Keskinen et al.*, 2003; *Kherani et al.*, 2005; *Sekar and Kelley*, 1998] have been devoted to the origin, evolution, and general characterization of equatorial ionospheric bubble structures. A major issue in equatorial ionospheric weather, in the form of spread-F bubble structures, is the identification of a precursor which would lead to the forecasting of equatorial ionospheric bubble development.

Experimental observations in the equatorial Pacific [*Tsunoda and White*, 1981; *Hysell et al.*, 2005] and South American regions [*Rodrigues et al.*, 2008; *Hysell and Burcham*, 1998; *Kudeki and Bhattacharyya*, 1999; *Woodman and LaHoz*, 1976] have demonstrated a strong correlation between large scale patchy wavelike layered structures in the bottomside F-region and the subsequent development of fully developed topside equatorial spread-F bubbles. In the equatorial Pacific sector, it was shown [*Tsunoda and White*, 1981] that, before equatorial bubble development,

distinctive large scale wavelike structures (LSWS) can occur in the bottomside F layer. The LSWS can occur over a large zonal distance of approximately 1200 km with an average zonal wavelength of 400 km. It was suggested that the LSWS are a precursor to equatorial spread-F bubbles. Similar observations were made in the equatorial Pacific region during the EQUIS II campaign [*Hysell et al*, 2005] which indicated bottomside layers at 200-250 km containing patchy structure with scale sizes in the range 30-150 km. In the equatorial South American sector, observations from the Jicamarca radar observatory [*Hysell and Burcham*, 1998; *Rodrigues et al.*, 2008] indicate that bottomside and bottom-type scattering are common especially during solar minimum and are precursors to large scale radar plumes that evolve at topside altitudes. Recently, large scale patchy structures have also been observed in Brazil [*Rodrigues et al.*, 2008] in the bottomside F-region preceding the onset of equatorial spread-F bubbles. In summary, experimental observations indicate a strong correlation between large scale wavelike patchy structure in the bottomside F-region and subsequent fully developed topside equatorial ionospheric bubbles. The altitudes of the bottomside patchy structures can be as low as 200 km during solar minimum periods with characteristic scale sizes of 30 - 400 km. They typically occur in regions below the steep F-region bottomside in the valley region. The patchy layers have not been observed when fully developed topside bubble structures are not observed.

Several models have been developed for these precursor wavelike patchy structures in the bottomside F-region. The collisional electrostatic Kelvin-Helmholtz instability, generated in the region of shear nodes in the F-region zonal flow, has been proposed [*Hysell and Kudeki*, 2004]. The gradient-drift instability, resulting from retrograde ionospheric flows in the bottomside region and zonal ionospheric density gradients, has been invoked [*Kudeki and Bhattacharyya*, 1999]. A sporadic-E layer instability has been discussed [*Tsunoda et al.*, 2006]. Gravity waves (GW) have also been proposed to directly excite the Rayleigh-Taylor instability in the steep bottomside F-region [*Kelley et al.*, 1981; *Huang and Kelley*, 1996; *Singh et al.*, 1997]. Recent results from the SpreadFEx campaign [*Fritts et al.*, 2008; *Taylor et al.*, 2009] have demonstrated the simultaneous observation [*Takahashi et al.*, 2009] of mesospheric gravity waves and equatorial ionospheric bubble structures. In addition, it has been shown [*Vadas et al.*, 2009; *Vadas*, 2007; *Vadas and Fritts*, 2005; *Keskinen and Vadas*, 2009] that large amplitude gravity waves from tropospheric sources can propagate into the E- and F-region ionosphere simultaneously. However, the nonlinear three-dimensional response of the bottomside ionosphere, at altitudes below the steep bottomside F-region gradient and shear node regions, to large amplitude dissipating gravity waves has not been studied in detail.

In this Letter, we compute the nonlinear response of the bottomside valley ionosphere to large amplitude dissipating gravity waves. It is found that large

amplitude bottomside F-region ionospheric density perturbations and polarization electric fields can be generated by such gravity waves. The outline of this Letter is as follows. In section 2 we present the model used to compute the ionospheric response to dissipating large amplitude gravity waves. In section 3 the principal results from this model are presented and compared with observations. Finally in section 4 the primary results of this study are summarized.

2. Model

The evolution of the equatorial ionospheric E and F regions can be described using the equations for the ionospheric plasma density, momentum, and current continuity

$$\frac{\partial n_\alpha}{\partial t} + \nabla \cdot n_\alpha \mathbf{V}_\alpha = P - L \tag{1}$$

$$\frac{e}{m_i}\left(\mathbf{E} + c^{-1}\mathbf{V}_i \times \mathbf{B}\right) - \nu_{ie}\left(\mathbf{V}_i - \mathbf{V}_e\right) - \nu_{in}\left(\mathbf{V}_i - \mathbf{U}\right) + \mathbf{g} = 0 \tag{2}$$

$$-\frac{e}{m_e}\left(\mathbf{E} + \frac{1}{c}\mathbf{V}_e \times \mathbf{B}\right) - \nu_{ei}\left(\mathbf{V}_e - \mathbf{V}_i\right) - \nu_{en}\left(\mathbf{V}_e - \mathbf{U}\right) = 0 \tag{3}$$

$$\nabla \cdot \mathbf{J} = \nabla \cdot \left[n\left(\mathbf{V}_i - \mathbf{V}_e\right)\right] = 0 \tag{4}$$

where α denotes ion or electron species, n_α the density, m_α the mass, ν_{in} the **ion-**neutral collision frequency, $\mathbf{U}$ is the thermospheric wind, ν_{ie}, ν_{ei} is the ion-electron and electron-ion Coulomb collision frequency, $\mathbf{E}$ the electric field with $\mathbf{E}_\perp = -\nabla_\perp \phi$ and $\mathbf{E}_\parallel = -\nabla_\parallel \phi$ and ϕ the electrostatic potential, $\mathbf{V}$ is the velocity, and $\mathbf{g}$ is gravity. For the E-region in Eq. (1), $\mathrm{P_E} = \mathrm{q_i}$ with q_i the photoionization rate. In addition,

the chemical loss terms in Eq. (1) can be modeled $\mathrm{L_E} = -\alpha \mathrm{n}_i^2$ and $\mathrm{L_F} = -\nu_\mathrm{R} \mathrm{n_i}$ with α and ν_R the E-region and F-region recombination rates, respectively. The electron gyrofrequency is taken to be large compared to the electron collision frequency and electron and ion inertial effects have been ignored. Using Eqs.(2)-(3), the total current **J** in Eq. (4) can be written as a sum of Pedersen, Hall, and parallel current contributions [*Keskinen et al.*, 2003; *Keskinen et al.*, 1998]. A cartesian coordinate system is adopted for simplicity with x-direction zonal (westward), z-direction meridional (north-south), and y-direction vertical, respectively. Magnetic field line curvature effects are not included.

Eq.(1)-(4) are solved for a three-dimensional volume extending from 100 - 250 km in altitude in the equatorial ionosphere. The simulated volume contains both the lower F region (150-250 km) and E-region (100-150 km). Since electric fields with transverse scale sizes greater than approximately 20 km are computed in the coupled model, the E-region will be strongly coupled to the F-region and vice versa [*Farley*, 1959]. It is assumed that the electric fields are electrostatic. For the modeled volume, Eq. (2)-(3) yield, to lowest order,

$$\mathbf{J}_\perp = \sigma_P \mathbf{E}_\perp^{'} - \sigma_H \mathbf{E}_\perp^{'} \times \hat{\mathbf{z}} \tag{5}$$

$$\mathbf{J}_\parallel = \sigma_\parallel \mathbf{E}_\parallel^{''} \tag{6}$$

where $\perp$ and $\parallel$ denote perpendicular and parallel to the ambient geomagnetic field,

respectively. The effective electric fields $\mathbf{E}^{'} = \mathbf{E}+(B/c\nu_i)(\mathbf{g}+\nu_i\mathbf{U})\times\hat{\mathbf{z}}$ and $\mathbf{E}_{\parallel}^{''} = \mathrm{E}_{\parallel}+(\mathrm{m}_e\nu_e/\mathrm{e})(1-\nu_{en}/\nu_e)\mathrm{U}_{\parallel}+(\mathrm{m}_e/\mathrm{e})(1-\nu_e/\nu_{in})g_{\parallel}$ include the polarization electric field and contributions from gravity and neutral motion. The Pedersen, Hall, and parallel conductivities are written $\sigma_p = \mathrm{ne}\mu_{i\perp}$, $\sigma_H = -\mathrm{ne}\mu_{iH}$, $\sigma_{\parallel} = \mathrm{ne}\mu_{e\parallel}$. The mobilities are given in standard form $\mu_{i\perp} = (c/B)\kappa_i/(1+\kappa_i^2)$, $\mu_{eH} = (c/B)\kappa_e^2/(1+\kappa_e^2)$, $\mu_{iH} = (c/B)\kappa_i^2/(1+\kappa_i^2)$, $\mu_{e\parallel} = c\kappa_e/B$, with $\nu_e = \nu_{en}+\nu_{ei}$, $\kappa_i = \Omega_i/\nu_i$, and $\kappa_e = \Omega_e/\nu_e$.

The current continuity condition can be written:

$$\nabla_{\perp}\cdot\mathbf{J}_{\perp}+\frac{\partial}{\partial z}J_{\parallel} = 0 \tag{7}$$

In detail, Eq. (7) can be written:

$$\begin{aligned}&\nabla_{\perp}\cdot\left[\sigma_p\left(\mathbf{E}+\frac{B}{c\nu_i}\mathbf{g}\times\hat{\mathbf{z}}\right)+\sigma_H\left(\mathbf{E}\times\hat{\mathbf{z}}+\frac{B}{c\nu_i}\mathbf{g}\right)\right]+\frac{\partial}{\partial z}\sigma_{\parallel}E_{\parallel}^{''}\\&=-\frac{B}{c}\left[\sigma_p\hat{\mathbf{z}}\cdot\nabla\times\mathbf{U}+\mathbf{U}\times\hat{\mathbf{z}}\cdot\nabla\sigma_p+\sigma_H\nabla_{\perp}\cdot\mathbf{U}+\mathbf{U}\cdot\nabla\sigma_H\right]\end{aligned} \tag{8}$$

The thermospheric winds act as a source term for the polarization electric fields in Eq. (8).

The ion continuity equation Eq. (1) is solved in the simulated volume to provide the ionospheric density in Eq. (8). Eq. (1) is written:

$$\frac{\partial n}{\partial t}+\nabla_{\perp}\cdot n\mathbf{V}_{i\perp}+\frac{\partial nV_{iz}}{\partial z} = P-L \tag{9}$$

with $\mathbf{V}_{i\perp} = \mu_{i\perp}\mathbf{E}_{\perp}^{'''}+\mu_{iH}\mathbf{E}_{\perp}^{'''}\times\hat{\mathbf{z}}$, $V_{iz} = \mu_{i\parallel}\mathrm{E}_{\parallel}^{'''}$, $\mu_{i\parallel} = c\kappa_i/B$, $\mathbf{E}_{\perp}^{'''} = \mathbf{E}_{\perp}+(B/c\Omega_i)(\mathbf{g}_{\perp}+\nu_i\mathbf{U}_{\perp})$ and $\mathrm{E}_{\parallel}^{'''} = \mathrm{E}_{\parallel}+(B/c\Omega_i)(\mathrm{g}_{\parallel}+\nu_i\mathrm{U}_{\parallel})$.

Eq. (8)-(9) are the model equations for the electrostatically coupled F- and E-region model and are solved numerically using computational techniques described previously [*Keskinen et al.*, 1998; *Keskinen et al.*, 2003] The background ionospheric and thermospheric profiles and parameters are found using IRI2001 and MSIS90E. Inhomogeneous thermospheric winds $\mathbf{U}_E$ in the E-region and lower F-region $\mathbf{U}_F$ make separate contributions to the total ionospheric polarization electric fields $\mathbf{E}$ from the current continuity equation (8). These polarization electric fields can then generate ionospheric density perturbations using Eq. (9).

3. Results

To compute the nonlinear lower ionospheric response to lower thermospheric gravity waves, we use the winds observed and modeled in the recent SpreadFEx campaign [*Vadas et al.*, 2009; *Keskinen and Vadas*, 2009]. In the SpreadFEx campaign, tropospheric convection was determined to be the most likely source for mesosphere and lower thermospheric GWs [*Vadas et al.*, 2009; *Takahashi et al.*, 2009].

Figure 1 shows the thermospheric wind, temperature, and density in the lower thermosphere from a GW source in the troposphere [*Vadas et al.*, 2009; *Keskinen and Vadas*, 2009]. The zonal horizontal GW wavelengths are in the range of 120 - 200 km with the vertical wavelengths approximately 20 - 90 km. In addition, Figure 1 also shows that the GW periods in the lower thermosphere from the tropospheric

source are approximately 18 min at the lowest altitudes and approximately 10 min at the higher altitudes. The GW model [*Vadas et al.*, 2009] yields maximum horizontal GW winds $u^{'}$ and vertical winds $w^{'}$, with amplitudes of approximately 150 m/sec and 100 m/sec, respectively, in the lower thermosphere. In addition, large thermospheric temperature $\mathrm{T}^{'}$ and density $\rho^{'}$ perturbations are generated from the GW model. The thermospheric winds are incorporated into the ionospheric model equations Eq. (8)-(9) assuming $\mathbf{U} = (\mathrm{U} + \mathrm{u}^{'})\hat{\mathbf{x}} + \mathrm{w}^{'}\hat{\mathbf{y}} + (\mathrm{V} + \mathrm{v}^{'})\hat{\mathbf{z}}$ where U,V are the mean zonal and meridional winds, respectively. The GW perturbation winds are taken to be of the form: $(\mathrm{u}^{'}, \mathrm{v}^{'}, \mathrm{w}^{'}) = (\mathrm{u}^{'}(\mathrm{y}), \mathrm{v}^{'}(\mathrm{y}), \mathrm{w}^{'}(\mathrm{y}))\cos(\mathrm{k}_x\mathrm{x} + \mathrm{k}_y\mathrm{y} + \mathrm{k}_z\mathrm{z} - \omega\mathrm{t})$ with $\omega = 2\pi/\tau$ and $\mathrm{k}_\beta = 2\pi/\lambda_\beta$ with $\beta = \mathrm{x}, \mathrm{y}, \mathrm{z}$.

Figure 2 displays the steady state ionospheric density perturbations in the F-region at t=135 min after imposing the thermospheric winds, temperatures, and density profiles Fig. 1. In addition to polarization electric field generation from the GW winds in Eq. (8), the GW effects on the recombination loss terms in Eq. (9) are also included [*Hooke*, 1968] with $\delta\alpha/\alpha = -1.2\mathrm{T}^{'}/\mathrm{T}$ for the E-region and $\delta\nu_R/\nu_R = \rho^{'}/\rho - \mathrm{T}^{'}/\mathrm{T}$. It is found that the F-region ionospheric density perturbations have both a large scale periodicity of approximately 120-150 km together with a smaller scale tilted patchy structure with scale size of 30-40 km. In addition, the ionospheric density perturbation amplitudes maximize in a layer-like structure at approximately 200 km in altitude. The ionospheric F-layer density

perturbation amplitudes can be as large as 43 %. The spatial k-spectra of the F-region density perturbations broaden in time so that a range of scale sizes are generated in the nonlinear regime. In comparison with experimental observations, Figure 3 gives an example of radar observations of bottom-type layered patchy structure at approximately 200 km in altitude [*Hysell et al.*, 2005] that typically precedes fully developed equatorial ionospheric plumes. The radar observations of the patchy structures in Figure 3 are coherent echoes of 1m ionospheric irregularities [*Hysell et al.*, 2005]. The minimum scale size in the model is approximately 1 km. The model ionospheric F-region density perturbations in Figure 2 are consistent with these observations if it is assumed that the radar data is a signature of the larger scale dynamics. Similar patchy layer structures have recently been observed [*Rodrigues et al.*, 2008].

Figure 4 shows the polarization electric fields computed from the nonlinear ionospheric model. It is found that the vertical electric fields are larger than the zonal electric fields. In addition, the zonal electric fields are found to be less structured than the vertical electric fields. The model results indicate that the polarization electric fields $\mathbf{E}$ are proportional to the combination of thermospheric GW wind vorticity ($\nabla \times \mathbf{U}$) and the wind divergence ($\nabla \cdot \mathbf{U}$) weighted by the Pedersen and Hall conductivity. The electric field magnitudes are also consistent with observations [*Hysell et al.*, 2005]. Similar polarization electric fields are also seen when the

model is initialized with a constant zonal electric field simulating the post sunset rise vertical drift.

4. Summary

A time-dependent nonlinear three-dimensionl model for the evolution of the equatorial bottomside lower ionosphere in the presence of dissipating gravity waves has been developed. Using the model it is found that large bottomtype F-region ionospheric density perturbations and electric fields can be driven by dissipating gravity waves from tropospheric sources. The spatial distribution of the ionospheric density perturbations can be characterized by a patchy, layer-like structure and may be responsible, in part, for observed large scale wavelike structures in the equatorial bottomside F-region which are a precursor to fully developed equatorial ionospheric bubbles. Favorable comparison of the model with observations is made.

Acknowledgments

This work was supported by NASA Living with a Star Targeted Research and Technology program. We thank Sharon Vadas and David Hysell for useful discussions.

References

Abdu, M.A., E. Kherani, I.S. Batista, R.R. de Paula, D.C. Fritts, and J.H.A. Sobral (2009), Gravity wave initiation of equatorial spread F/plasma bubble irregularities based on observational data from the SpreadFEx campaign, *Ann. Geophys., 27*, 2607.

Bhattacharyya, A., Role of E-region conductivity in the development of equatorial ionospheric plasma bubbles (2004), *Geophys. Res. Lett., 31*, L06806, doi:10.1029/2003GL018960.

Farley, D.T., A theory of electrostatic fields in a horizontally stratified ionosphere subject to a vertical magnetic field, *J. Geophys. Res., 64*, 1225, 1959.

Fritts, D.C., S.L. Vadas, D.M. Riggin, M.A. Abdu, I.S. Batista, H. Takahashi, A. Medeiros, F. Kamalabadi, H.-L. Liu, B.G. Fejer, and M.J. Taylor, Gravity wave and tidal influences on equatorial spread F based on observations during the Spread F experiment (SpreadFEx), Ann. Geophys., 26, 3235, 2008.

Hocke, K. and T. Tsuda, Gravity waves and ionospheric irregularities over tropical convection zones observed by GPS/MET radio occultation, *Geophys. Res. Lett., 28*, 2815, 2001.

Hooke, W.H., Ionospheric irregularities produced by internal atmospheric gravity waves, *J. Atmos. Terr. Phys., 30*, 795, 1968.

Huang, C.S., and M.C. Kelley (1996), Nonlinear evolution of equatorial spread-F: 1.

On the role of plasma instabilities and spatial resonance associated with gravity wave seeding *J. Geophys. Res., 101*, 238.

Huba, J.D. G. Joyce, J, Krall (2008), Three-dimensional equatorial spread-F modeling *Geophys. Res. Lett., 35*, L10102, doi:10.1029/2008GL033509.

Hysell, D.L., and E. Kudeki (2004), Collisional shear instability in the equatorial F region ionosphere *J. Geophys. Res., 109*, A11301, doi:10.1029/2004JA0106636.

Hysell, D.L., M.F. Larsen, C.M. Swenson, A. Barjatya, T.F. Wheeler, M.F. Sarango, R.F. Woodman, and J.L. Chau (2005), Onset conditions for equatorial spread-F determined during EQUIS II, *Geophys. Res. Lett., 32*, L24104, doi:10.1029/2005GL024743.

Hysell, D.L., and J. Burcham (1998), JULIA radar studies of equatorial spread F, *J. Geophys. Res., 103*, 29155.

Kelley, M.C., M.F. Larsen, C. LaHoz, and J.P. McClure (1981), Gravity wave initiation of equatorial spread-F: A case study, *J. Geophys. Res., 86*, 9087.

Keskinen, M.J., S.L. Ossakow, and B.G. Fejer (2003), Three-dimensional nonlinear evolution of equatorial ionospheric spread-F bubbles, *Geophys. Res. Lett., 30*(16), 1855, doi:10.1029/2003GL017418.

Keskinen, M.J., S.L. Ossakow, S. Basu, and P.J. Sultan (1998), Magnetic-flux-tube-integrated evolution of equatorial ionospheric plasma bubbles, *J. Geophys. Res., 103*, 3957.

Keskinen, M.J., and S.L. Vadas(2009), Three-dimensional nonlinear evolution of

equatorial ionospheric bubbles with gravity wave seeding and tidal wind effects, *Geophys. Res. Lett., 36*, L12102, doi:10.1029/2009GL037892.

Kherani, E.A., M. Mascarenhas, J.H.A. Sobral, E.R. dePaula, and F.C. Bertoni (2005), A three-dimensional model of collisional interchange instability, *Space Sci. Rev. 121*, 253.

Kil, H., R. DeMajistre, and L.J. Paxton (2004), F-region distribution seen from TIMED/GUVI and its relation to equatorial spread-F activity, *Geophys. Res. Lett., 31*, L05810, doi:10.1029/2003GL018703.

Kudeki, E. and S. Bhattacharyya (1999), Post-sunset vortex in equatorial F-region plasma drifts and implications for bottomside spread-F, *J. Geophys. Res., 104*, 28163.

Rodrigues, F.S., D.L. Hysell, and E.R. dePaula, Coherent backscatter radar imaging in Brazil: large scale waves in the bottomside F-region at the onset of equatorial spread F, Ann. Geophys, 26, 3355, 2008.

Sekar, R., and M.C. Kelley (1998), On the combined effects of vertical shear and zonal electric field patterns on nonlinear equatorial spread F evolution, *J. Geophys. Res., 103*, 20735.

Singh, S., F.S. Johnson, and R.A. Power (1997), Gravity wave seeding of equatorial plasma bubbles, *J. Geophys. Res., 102* A4, 7399.

Straus, P.R., P.C. Anderson, and J.E. Danaher (2003), GPS occultation sensor ob-

servations of ionospheric scintillation, *Geophys. Res. Lett.*, 10.1029/2002GL016503.

Takahashi, H., et al. (2009), Simultaneous observation of ionospheric plasma bubbles and mesospheric gravity waves during the SpreadFEx campaign, *Ann. Geophys, 27*, 1477.

Taylor, M.J., P.D. Pautet, A.F. Medeiros, R. Buriti, J. Fechine, D.C. Fritts, S.L. Vadas, H. Takahashi, and F.T. Sao Sabbas, Characteristics of mesospheric gravity waves near the magnetic equator during the SpreadFEx campaign, *Ann. Geophys, 27*, 461, 2009.

Tsunoda, R.T. (2006), Day-to-day variability in equatorial spread-F: is there some physics missing?, *Geophys. Res. Lett., 33*, L16106, doi:10.1029/2006GL025956.

Tsunoda, R.T., and B.R. White, On the generation and growth of equatorial backscatter plumes: 1, wave structure in the bottomside F layer, *J. Geophys. Res., 86*, 3610, 1981.

Vadas, S.L. (2007), Horizontal and vertical propagation and dissipation of gravity waves in the thermosphere from lower atmospheric and thermospheric sources, *J. Geophys. Res., 112*, A06305, doi:10.1029/2006JA011845.

Vadas, S.L., and D.C. Fritts (2005), Thermospheric responses to gravity waves: influences of increasing viscosity and thermal diffusivity, *J. Geophys. Res., 110*, D15103, doi:10.1029/2004JD005574.

Vadas, S.L., M.J. Taylor, P.D. Pautet, P.A. Stamus, D.C. Fritts, H.-L. Liu, F.T.

Sao Sabbas, V.T. Rampinelli, P. Batista, and H. Takahashi, Convection: the likely source of the medium scale gravity waves observed in the OH airglow layer near Brasilia, Brazil during the SpreadFEx campaign, *Ann. Geophys., 27*, 231, 2009.

Woodman, R.F., and C. LaHoz (1976), Radar observations of F region equatorial irregularities, *J. Geophys. Res., 81*, 5447.

Figure Captions

Figure 1 Altitude dependence of (a) GW zonal (bold), vertical (dashed) and meridional (dash-dot) wavelengths, (b) mean zonal U (bold) and GW zonal $u^{'}$ (dashed), (c) mean meridional V (bold) and GW meridional $v^{'}$ (dashed), (d) GW vertical $w^{'}$ (bold), (e) GW periods τ, (f) % GW temperature perturbations $T^{'}/T$ and GW density perturbations $\rho^{'}/\rho$.

Figure 2 Vertical and horizontal dependence of relative F-region ionospheric density perturbations $\delta n_F/n_{F0}$ in the equatorial plane at t=135 min. Here n_{F0} is the background ionospheric density profile at t=0.

Figure 3 Experimental radar observations of bottom-type scattering layer at approximately 200 km altitude (from *Hysell et al.*, 2005) preceding the onset of equatorial spread F plumes.

Figure 4 Altitude dependence of zonal E_x and vertical E_y polarization electric fields.

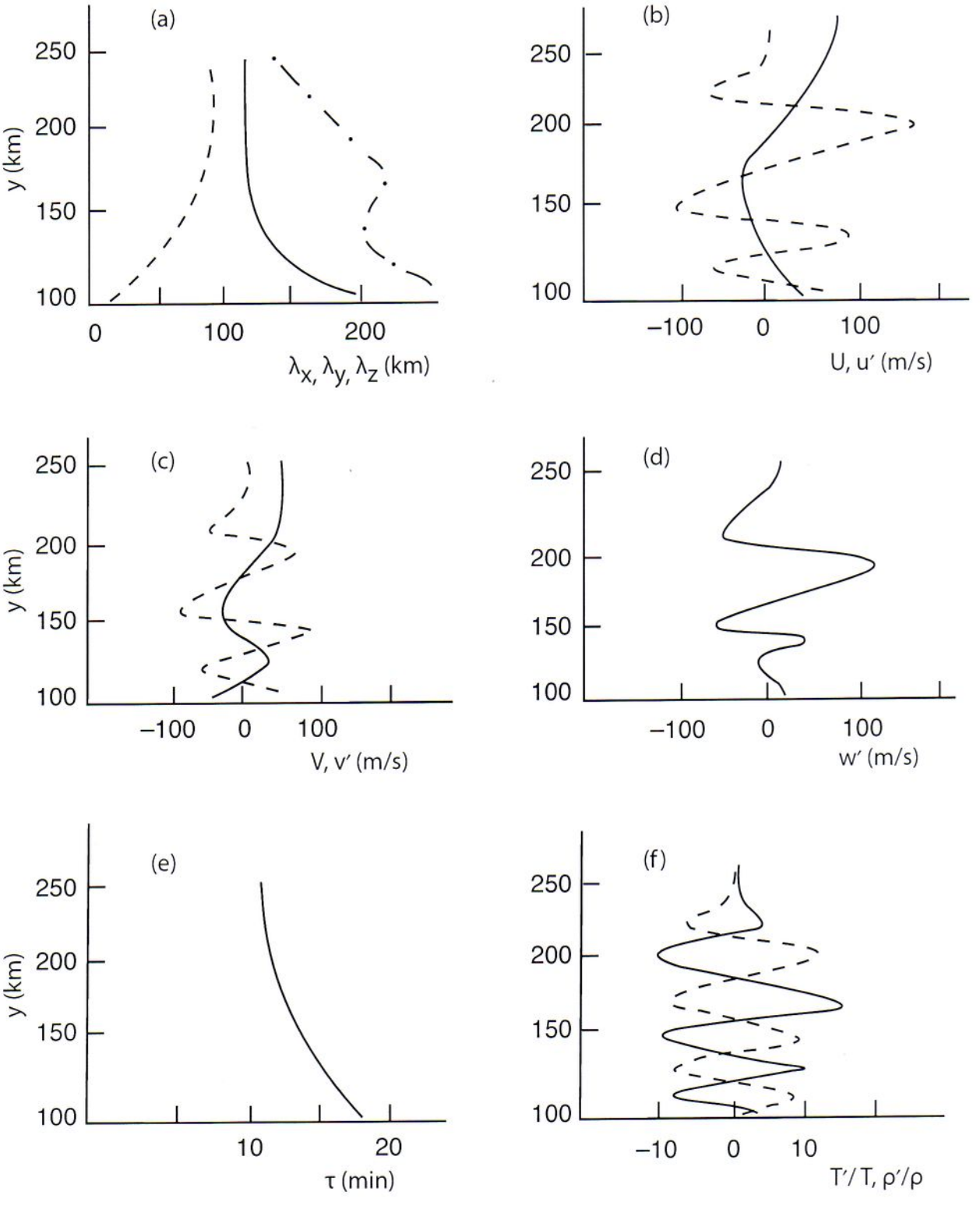
(a)
y (km)
250
200
150
100
0
100
200
λx, λy, λz (km)
(b)
250
200
150
100
−100
0
100
U, u′ (m/s)
(c)
y (km)
250
200
150
100
−100
0
100
V, v′ (m/s)
(d)
250
200
150
100
−100
0
100
w′ (m/s)
(e)
y (km)
250
200
150
100
10
20
τ (min)
(f)
250
200
150
100
−10
0
10
T′/T, ρ′/ρ

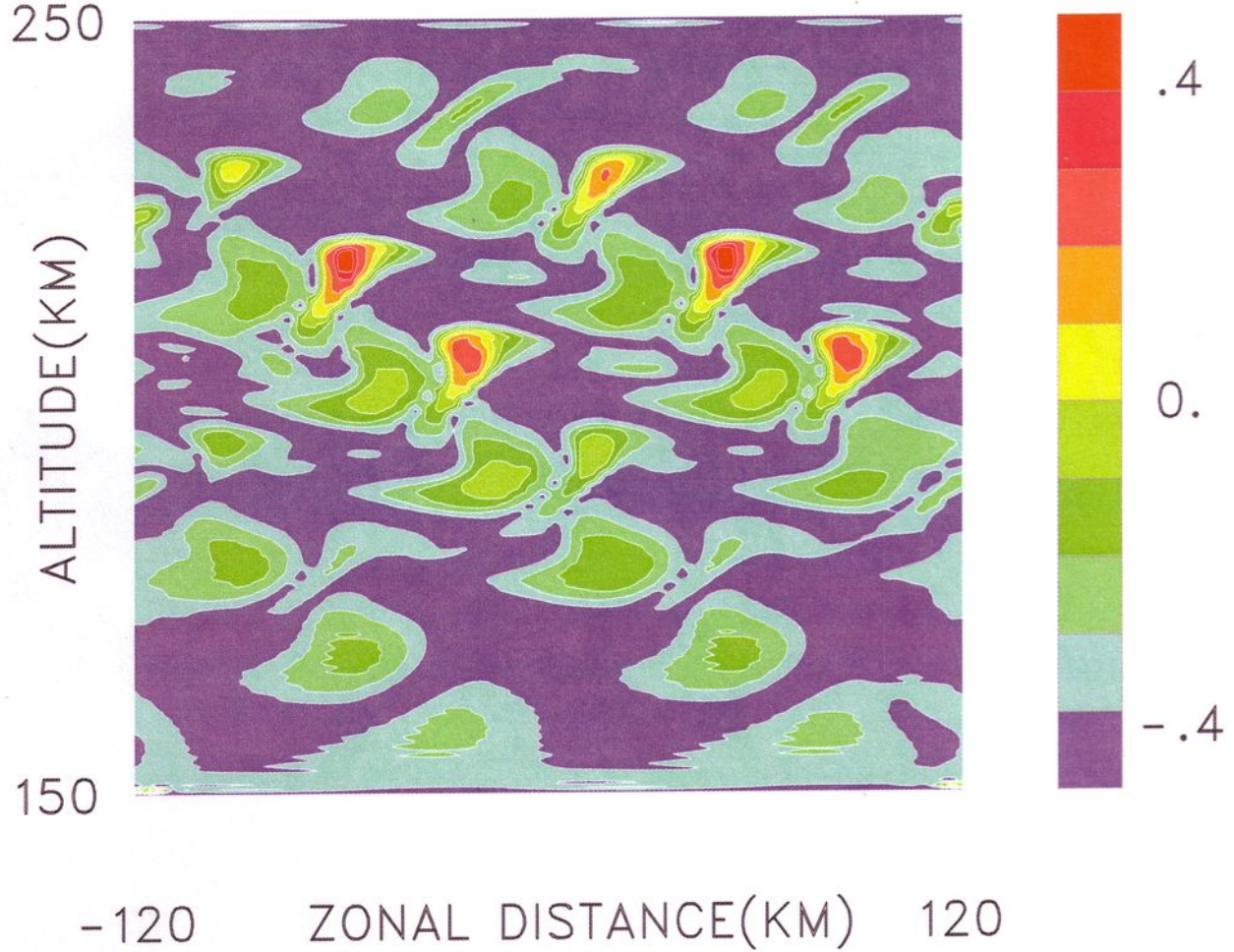
250
ALTITUDE(KM)
150
.4
0.
-.4
-120
ZONAL DISTANCE(KM)
120

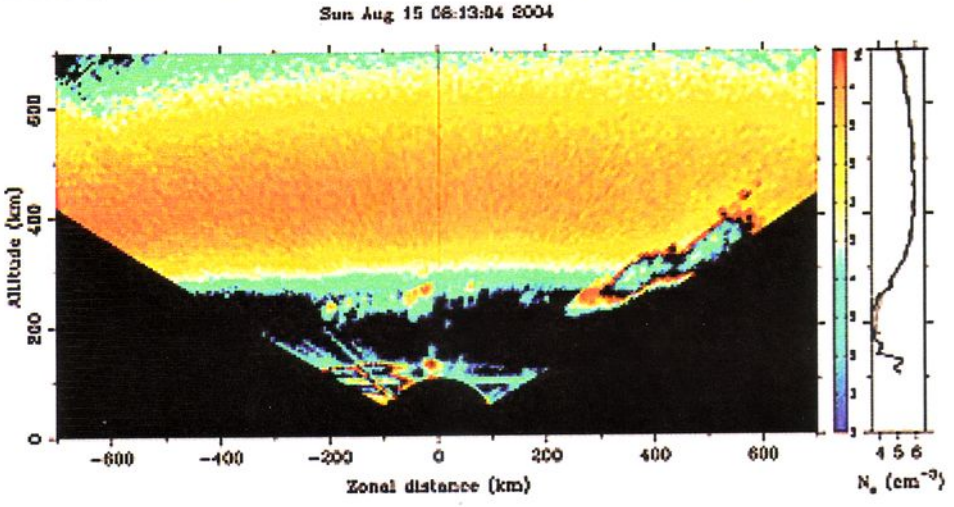
Sun Aug 15 06:13:04 2004
Altitude (km)
0
200
400
600
-600
-400
-200
0
200
400
600
Zonal distance (km)
4 5 6
N_e (cm^{-3})

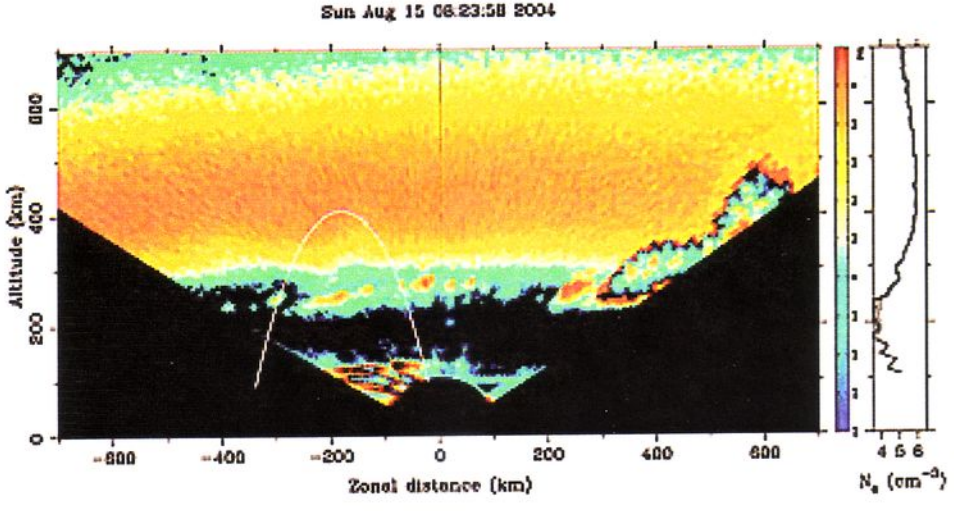
Sun Aug 15 06:23:58 2004
Altitude (km)
0
200
400
600
-600
-400
-200
0
200
400
600
Zonal distance (km)
4 5 6
N_e (cm^{-3})

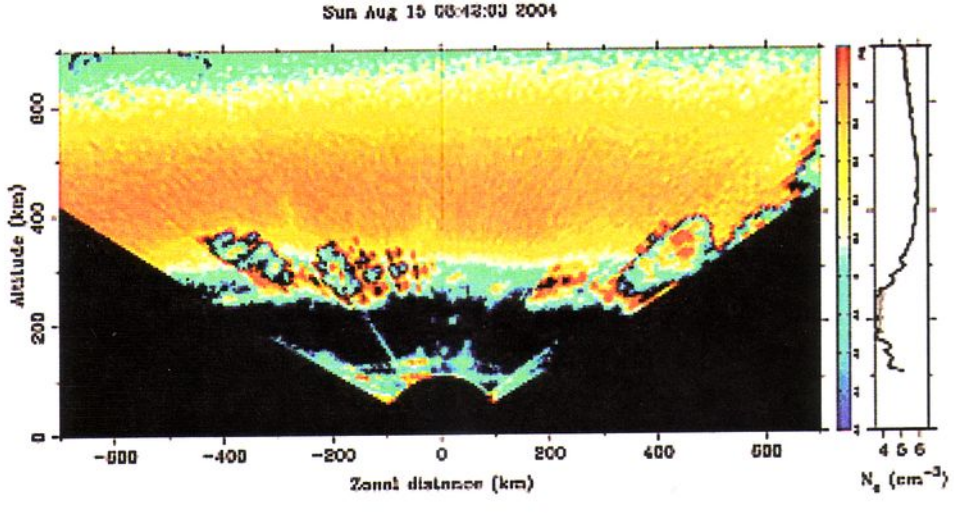
Sun Aug 15 06:43:03 2004
Altitude (km)
0
200
400
600
-600
-400
-200
0
200
400
600
Zonal distance (km)
4 5 6
N_e (cm^{-3})

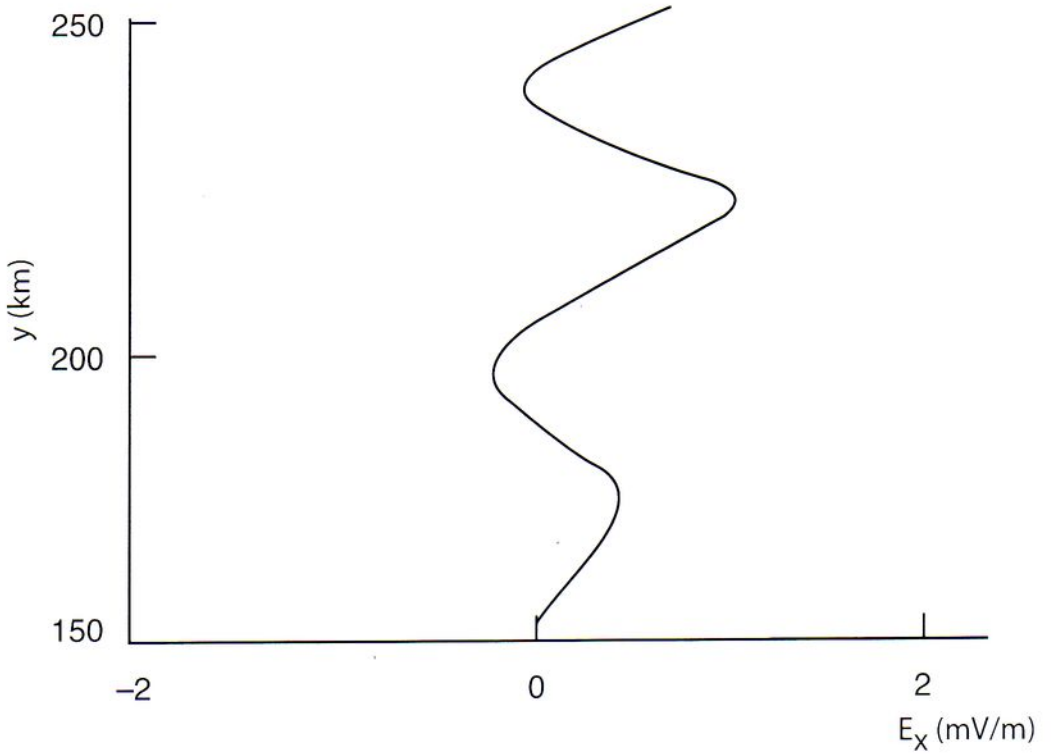
250
200
150
y (km)
–2
0
2
E_x (mV/m)

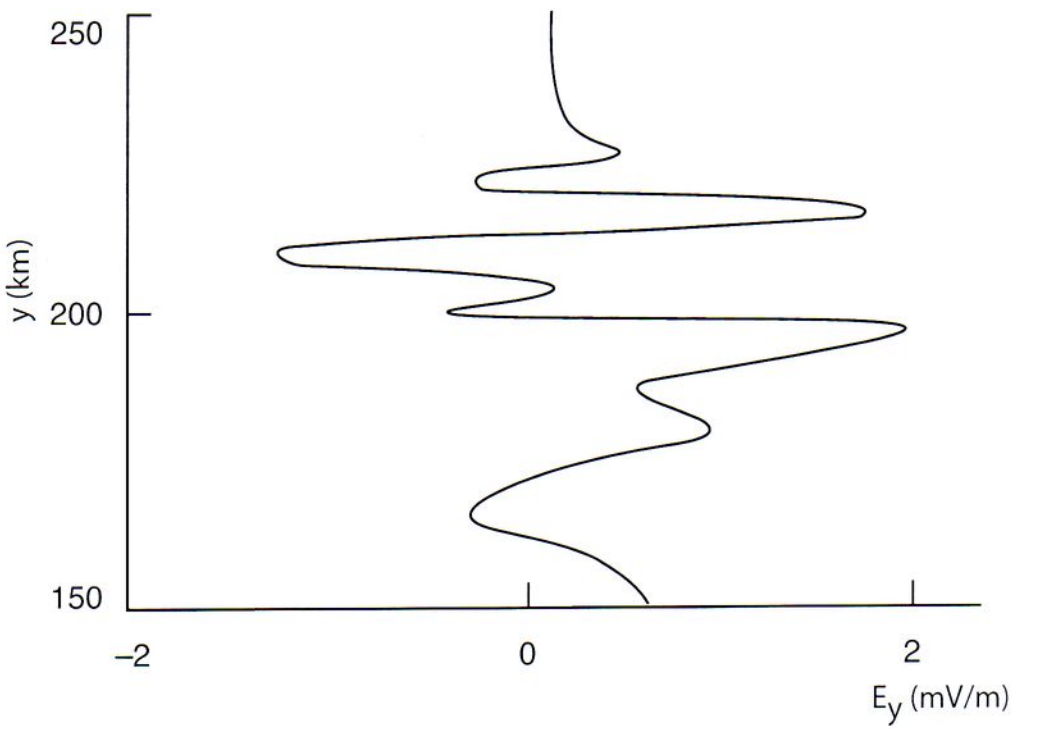
250
200
150
y (km)
–2
0
2
E_y (mV/m)